Pore-merging methodology for reactive transport and mineral dissolution in pore-network models

Barbara F. Esteves [a,b], Paulo L.C. Lage [a], Paulo Couto [c], Anthony R. Kovscek [*,b]

[a] Programa de Engenharia Química (PEQ/COPPE), Universidade Federal do Rio de Janeiro, Rio de Janeiro, RJ, 21941-972, Brazil
[b] Energy Resources Engineering, Stanford University, Stanford, CA, 94305, USA
[c] Programa de Engenharia Civil (PEC/COPPE), Universidade Federal do Rio de Janeiro, Rio de Janeiro, RJ, 21941-972, Brazil

A B S T R A C T

This study proposes a pore-network modeling algorithm to simulate single-phase reactive transport and mineral dissolution in porous media. A novel pore-merging approach is introduced to guarantee the conservation of the most critical variables during the merging process by using correction factors and effective properties for throat conductances and surface areas. Our approach solves a coupled transport and reaction pore-network model that implements a kinetic model with a single heterogeneous chemical reaction describing the dissolution of calcite by acidic solutions. The network geometry is updated based on the dissolution process occurring at the mineral surface and the network topology is updated based on the pore-merging processes occurring throughout the network. The main results include the exploration of different dissolution regimes through porosity-permeability evolution curves, acid concentration profiles, and the use of statistical criteria. Importantly, this methodology simulates permeability increases larger than 100-fold during the formation of preferential pathways (i.e., wormholes).

1. Introduction

Reactive transport and mineral dissolution in porous media are fundamental processes in many subsurface applications, including carbon dioxide (CO_2) storage, enhanced oil recovery (EOR), and acidizing for stimulation (Sohrabi et al., 2012; Wolterbeek and Raoof, 2018; Menke et al., 2018; Gharbi et al., 2013).

For example, CO_2 injection into reservoirs triggers the occurrence of chemical reactions that induce changes in mechanical properties of the rock, especially in porous media rich in carbonate minerals (Egermann et al., 2010; Rathnaweera et al., 2016; Bemer and Lombard, 2010). Regarding geological CO_2 storage, these structural alterations are a source of concern for the safety and efficiency of the process due to the increase of the chances for leakage and CO_2 migration out of the storage formation (Deng et al., 2017; Egermann et al., 2010; Rathnaweera et al., 2016; Bemer and Lombard, 2010). Indeed, depending on the dominant transport mechanism, poor utilization of the pore space for the storage of CO_2 may occur (Ott and Oedai, 2015). Regarding acidizing for well stimulation, the main goal is to increase well productivity. The formation of preferential pathways is desired to increase the overall conductance through the reservoir (Hill and Schechter, 2000; Ott and Oedai, 2015; Fredd and Fogler, 1999).

Accordingly, good understanding of the dissolution processes is imperative to assess long-term reservoir integrity properties for CO_2 storage and to design efficiently acidizing treatments (Rathnaweera et al., 2016; Bemer and Lombard, 2010; Fredd and Dowell, 2000). In order to investigate the dissolution processes in porous media, several numerical approaches, such as direct numerical simulations (DNS) that include computational fluid dynamics (CFD) (Soulaine et al., 2017; Oliveira et al., 2019; Molins et al., 2012), lattice Bolzmann method (LBM) (Liu and Mostaghimi, 2017; Kang et al., 2002; Huber et al., 2014), smoothed particle hydrodynamics (SPH) (Tartakovsky et al., 2016), and approaches that consider a simplified conceptualization of the porous media, commonly associated with pore-network modeling (PNM), have been developed (Esteves et al., 2020; Li et al., 2006; Algive et al., 2010; Raoof et al., 2012; Tansey and Balhoff, 2016; Budek and Szymczak, 2012). An overview of the various numerical approaches applied to pore-scale mineral dissolution are found in Molins et al. (2020).

Pore network modeling is a technique that is widely used to represent natural porous media and complex pore geometries using a simplified pore-and-throat type network (Algive et al. 2010). Since the pioneering work of Fatt (1956), that studied two-phase flow and capillary pressure curves, pore-network models have been successfully

---

* Corresponding author.
  E-mail addresses: besteves@stanford.edu (B.F. Esteves), kovscek@stanford.edu (A.R. Kovscek).

Nomenclature

z	Coordination number
q_{ij}	Volumetric flow rate through throat ij
$c_{e,ij}$	Effective conductance of throat ij
ϵ_{ij}	Correction factor for the conductance of throat ij
r_{ij}	Cross-section radius of the throat ij
μ	Dynamic viscosity of the fluid
l_{ij}	Length of the throat ij
K	Absolute permeability of the network
ΔP	Pressure difference through the network
A	Cross-sectional area of the network
L	Length of the network
$A_{\psi,i}$	Effective surface area of pore i
$A_{\psi,ij}$	Effective surface area of throat ij
ψ_i	Surface area correction factor of pore i
ψ_{ij}	Surface area correction factor of throat ij
t	Time
$C_{\alpha,i}$	Mass concentration of species α in pore i
$C_{\alpha,ij}$	Mass concentration of species α in throat ij
V_i	Volume of pore i
$\mathscr{D}_\alpha$	Diffusion coefficient of species α
r_i	Radius of pore i
$R_{\alpha,i}$	Reaction rate of specie α due to heterogeneous chemical reaction in pore i
$R_{\alpha,ij}$	Reaction rate of specie α due to heterogeneous chemical reaction in throat ij
δV_i^d	Change in volume due to dissolution process in pore i
δV_{ij}^d	Change in volume due to dissolution process in throat ij
δr_i^d	Change in radius of pore i due to dissolution process
δr_{ij}^d	Change in radius of throat ij due to dissolution process
$\delta V_{i,ij}^{dd}$	Change in volume due to double dissolution in the region between pore i and throat ij
δV_i^{dd}	Total change in volume due to double dissolution for pore i
δV_{ij}^{dd}	Total change in volume due to double dissolution for throat ij
δr_i^{dd}	Change in radius of pore i due to double dissolution
$\delta V_{i,ij}^{c1}$	Change in volume due to correction 1 in the region between pore i and throat ij
δV_i^{c1}	Total change in volume due to correction 1 for pore i
δV_{ij}^{c1}	Total change in volume due to correction 1 for throat ij
δr_i^{c1}	Change in radius of pore i due to correction 1
$\delta V_{i,ij}^{c2}$	Change in volume due to correction 2 in the region between pore i and throat ij
δV_i^{c2}	Total change in volume due to correction 2 for pore i
δV_{ij}^{c2}	Total change in volume due to correction 2 for throat ij
δr_i^{c2}	Change in radius of pore i due to correction 2
$\delta V_{i,ij}^{t}$	Volume of the porous region previouly belonging to throat ij transferred to pore i
$\delta m_{i,ij}^{t}$	Mass of acid in the porous region previouly belonged to throat ij transferred to pore i
δV_i^{t}	Total change in volume due to porous space transfer from throat ij to pore i, for pore i
δV_{ij}^{t}	Total change in volume due to porous space transfer from throat ij to pore i, for throat ij
δm_i^{t}	Total change in mass of acid due to porous space transfer from throat ij to pore i, for pore i
δm_{ij}^{t}	Total change in mass of acid e due to porous space transfer from throat ij to pore i, for throat ij
$\mathbf{x}$	Position vector
$\mathbf{x}$	
d_{mk}	Interpore distance between the newly merged pore m and the connected pore k
r_m^{n+1}	Radius of the newly merged pore m
r_k^{n+1}	Radius of the pore k connected to the new merged pore m
r_{mk}^{n+1}	Radius of the newly throat connecting the merged pore m and the connected pore k
$A_{r,mk}^{n+1}$	Reactive surface area of the newly throat connecting the merged pore m and the connected pore k
c_{mk}^{n+1}	Conductance of the newly throat connecting the merged pore m and the connected pore k
ψ_{mk}^{n+1}	Correction factor of the newly throat connecting the merged pore m and the connected pore k
σ_{cs}	Standard deviation of cross section cs
CV_{cs}	Coefficient of variation of cross section cs
CV	Averaged coefficient of variation
ΔC	Measure of the consumption of acid along the network
δV_i	Total change in volume of pore i
δV_{ij}	Total change in volume of throat ij

applied in numerous research areas, including reactive transport and mineral dissolution problems (Li et al., 2006; Algive et al., 2010; Raoof et al., 2012; Tansey and Balhoff, 2016; Esteves et al., 2020). The computational efficiency of pore-network models is related to the simplicity of their geometry and because of this feature, pore-network modeling is considered applicable to much larger domains when compared to direct simulation methods (Mehmani and Balhoff, 2015; Yang et al. 2016).

In this context, merging of pores and throats to form vug-like pores is needed to evaluate better regimes with significant mineral reactivity. The appropriate treatment of pore merging allows a better representation of the physical problem and makes possible the use of reactive transport simulations to evaluate dissolution regimes in more complex network topologies, where the merging of pores is likely to occur with great frequency due to the heterogeneity of these type of porous media. Few pore-network modeling studies explored the use of pore-merging methods to explore mineral dissolution in porous media.

Budek and Szymczak (2012) performed the first pore-network study that considered an approach to merge pores during reactive transport and mineral dissolution. The porous medium was represented by a two-dimensional triangular network of cylindrical tubes. The points where the tubes meet are referred to as nodes. In this way, pores are defined just as node points for pressure determination. Then, throats are tubes that enlarge during the dissolution process. Note that a single reactant is assumed to describe approximately the carbonate dissolution.

Their methodology for merging considers that, as the diameters of the eroding throats become comparable to the interpore distances, the throats are joined together. The assumption is that the new throat has the same diameter as the sum of the diameters of the original two throats. With this, the reactive surface area is conserved during the merging process, but the volume is not.

Tansey and Balhoff (2016) developed a pore network model of heterogeneous reactive transport and matrix dissolution that considers a pore-merging criterion to improve the pore-scale physics of the network. Simulations were conducted on random close-pack arrangements of spheres and the transport equation assumes pores as the only control volumes. Throats represent the conductances throughout the network.

This approach also assumes the tracking of only one chemical species and the reactive transport equation is solved explicitly.

During simulation, pores grow assuming a static geometry by preserving the relation between surface area and volume. Throat cross-section areas are updated based on the new surface area of the connected pores. Throat conductances are then updated based on the new cross-sectional areas, also assuming a static geometry using a shape factor to map the throat shape onto a cylindrical tube and preserving initial relationships between throat cross section and conductivity. The merging approach developed by Tansey and Balhoff (2016) assumes that the new merged pore's volume is equal to the combined volume of both original pores.

The use of a merging criterion by Tansey and Balhoff (2016) showed the importance of capturing the formation of preferential pathways. Without merging of overlapping pores, permeability could not increase past a small fraction of its potential, reaching a plateau with no occurrence of wormholes (Tansey and Balhoff, 2016).

Clearly, significant insights and improvements were achieved by these studies, although some strong simplifications were assumed related to the evolution of geometry during dissolution and merging processes. Assuming static relations between surface areas and volumes may not be the best representation for all the different dissolution regimes, because pores and throats may be affected differently.

The conservation of geometry and flow properties during the application of a merging strategy is paramount to maintain a continuous evolution of porous media due to the dissolution process. The structure of the network before and after two overlapping pores merge must be represented in a manner faithful to the physical problem and include a minimum of unrealistic simplifications.

Maintenance of the available reactive surface area and volume of the overlapping pores, as well as conductivity of the connected throats, are essential for an accurate evaluation of the dissolution regimes. Transport phenomena and reaction within the pore spaces are highly dependent on these properties. Therefore, the main objective of this study is to develop a new methodology to describe the merging of pores and throats resulting from solid matrix dissolution during single-phase flow that guarantees the conservation of the main variables of interest, namely porous volume, mass of acid, reactive surface area, and throat conductances. Surface areas and conductances are modeled using a novel application of correction factors and effective properties. Thus, the conservation of these properties is possible during the merging process, in addition to the volume and mass of acid already conserved. This approach aims to bring pore-network models closer to the physical problem and make possible reactive transport simulations to evaluate dissolution regimes in more complex network topologies. In such networks, the odds for the junction of two pore spaces initially separated increases due to the heterogeneity in pore sizes.

2. Methodology

This section first presents the equations to determine the pressure and concentration fields. The kinetics of dissolution and the evolution of the volumes and geometry of a stick-and-ball network are also described. Then, the new pore-merging approach to describe dissolving pores is introduced. Finally, definition of the dimensionless numbers and the statistical criteria are presented. The pore-network models used for this study are presented at the end of this section.

2.1. Pressure field

The pseudo steady-state flow of a single-phase incompressible fluid is assumed in order to obtain the pressure field of the network. The mass conservation for each pore is given by

$$\sum_{ij}^{z} q_{ij} = 0, \tag{1}$$

where z is the coordination number and q_{ij} is the volumetric flow rate through throat ij. The volumetric flow rate through a pore-throat is determined by the pressure difference between the connected pores i and j $(P_i - P_j)$ and the throat effective conductance $(c_{\epsilon,ij})$, as follows

$$q_{ij} = c_{\epsilon,ij}(P_i - P_j). \tag{2}$$

Note that throat volumetric flow rates are obtained using the effective conductance instead of the conductance derived only from geometrical data. Effective conductances assure that the relationship between flow rate through pores and the extent of dissolution is represented accurately after merging. The effective conductance $(c_{\epsilon,ij})$ is described by

$$c_{\epsilon,ij} = \epsilon_{ij} c_{ij}, \tag{3}$$

where ϵ_{ij} is the conductance correction factor. The conductance correction factor is equal to 1 for all original throats, and the value is updated when the throat ij is involved in a merging process. Thus, initially, the effective conductance is equal to the conductance.

The throat conductance is obtained by use of Poiseuille's law for laminar flow in a cylindrical tube:

$$c_{ij} = \frac{\pi r_{ij}^4}{8 \mu l_{ij}}, \tag{4}$$

where r_{ij} is the radius of throat ij cross-section, μ is the dynamic viscosity of the fluid and l_{ij} is the length of the throat ij.

Substituting Eqs. (2) and (4) into Eq. (1), a linear algebraic system for the unknown pressure field is solved for the pressure in each pore. Constant volumetric flow rate at the inlet boundary and fixed pressure at the outlet boundary are imposed to determine the pseudo steady-state flow field of the network. Fixed pressures are imposed at the inlet and outlet boundaries to determine the absolute permeability. All other boundaries are closed. Therefore, both cases are one-dimensional flow problems. Considering the last case, the total flow rate through the network (Q) is obtained after pressure field determination and Darcy's law is used to calculate the absolute permeability (K) of the system, as described below

$$K = \frac{\mu Q L}{A \Delta P}, \tag{5}$$

where A is the cross-sectional area of the network and L is the length of the network.

2.2. Concentration field

The reactive transport problem is described by the mass balance in all available pore spaces, pores and throats, and is deduced from the mass conservation equations of the chemical species (Bird et al., 2007). This new approach uses effective surface areas instead of the reactive surface areas obtained just by geometrical information.

The effective surface area is the geometrical reactive surface area corrected by a correction factor due to merging, as presented below:

$$A_{\psi,i} = \psi_i A_{r,i}, \tag{6}$$

$$A_{\psi,ij} = \psi_{ij} A_{r,ij}. \tag{7}$$

where $A_{\psi,i}$ is the effective surface area of pore i, $A_{\psi,ij}$ is the effective surface area of throat ij, ψ_i is the surface area correction factor of pore i and ψ_{ij} is the surface area correction factor of throat ij.

Thus, original pores and throats have surface area correction factors equal to 1. The correction factor of a pore space is just updated if it is
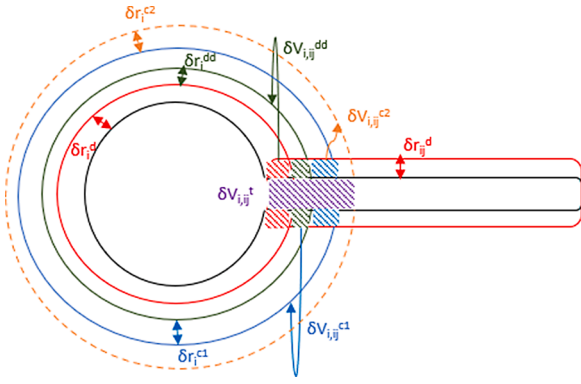
Fig. 1. Scheme of the evolution of pore and throat volumes during dissolution. Hatched area in red represents the region of double dissolution ($\delta V_{i,ij}^{dd}$). Hatched areas in green and blue represent, respectively, the region of the first correction step ($\delta V_{i,ij}^{c1}$) and the region of the second correction step ($\delta V_{i,ij}^{c2}$). Hatched area in purple represents the porous region of throat ij that is transferred to pore i ($\delta V_{i,ij}^{t}$). (For interpretation of the references to colour in this figure legend, the reader is referred to the web version of this article.)

involved in a merging process. So, until a merging event occurs, the effective surface area of a pore space is equal to its geometrical surface area, obtained by Eqs. (A.15) and (A.12), respectively for pores and throats. Implementation of correction factors ensures that surface area and conductance evolve in a physically realistic manner. More details about the update of surface area correction factors are available in later sections.

The transport of a chemical species occurs by advection and diffusion. The mass balance equation for chemical species α in a spherical pore i is

$$\frac{d}{dt}\left(C_{\alpha,i} V_i\right) = \sum_{ij,in} C_{\alpha,ij} q_{ij} - C_{\alpha,i} \sum_{ij,out} q_{ij}$$
$$+ \sum_{ij} A_{ij} \mathscr{D}_\alpha \left(\frac{C_{\alpha,ij} - C_{\alpha,i}}{0.5 l_{ij} + r_i}\right) - R_{\alpha,i} A_{\psi,i}, \tag{8}$$

where t is the time, $C_{\alpha,i}$ is the mass concentration of species α in pore i, $C_{\alpha,ij}$ is the mass concentration of species α in throat ij, V_i is the volume of pore i, A_{ij} is the cross-sectional area of throat ij, $\mathscr{D}_\alpha$ is the diffusion coefficient of species α, r_i is the radius of pore i, $R_{\alpha,i}$ is the reaction rate of species α due to heterogeneous chemical reaction in pore i.

For control volumes represented by cylindrical throats ij, the mass balance equation for species α is

$$\frac{d}{dt}\left(C_{\alpha,i} V_{ij}\right) = \left(C_{\alpha,i} - C_{\alpha,ij}\right) q_{ij} + A_{ij} \mathscr{D}_\alpha \left(\frac{C_{\alpha,i} - C_{\alpha,ij}}{0.5 l_{ij} + r_i}\right)$$
$$+ A_{ij} \mathscr{D}_\alpha \left(\frac{C_{\alpha,j} - C_{\alpha,ij}}{0.5 l_{ij} + r_j}\right) - R_{\alpha,ij} A_{\psi,ij}, \tag{9}$$

where $C_{\alpha,i}$ is the mass concentration of species α in the pore from where the flow is arriving in the throat ij.

In our approach, the concentration field is solved implicitly and the volume explicitly in a sequential algorithm. In other words, the system is solved for the new concentrations based on the previous geometry, that is kept constant during the solution of Eqs. (8) and (9). The linear system for the unknown concentrations of species α is solved by *spsolve* direct method from the SciPy library (Jones et al., 2001). The domain initial condition considers a constant concentration profile and the domain boundary conditions consider a constant concentrations for the inlet pore-spaces and an outflow boundary condition for the outlet pores.

2.3. Dissolution kinetics

During the dissolution process, porous medium geometry and topology evolves with heterogeneous chemical reactions at the effective surface areas of pores and throats. Our approach solves a coupled transport and reaction pore-network model that implements a kinetic model with a single heterogeneous chemical reaction describing the dissolution of calcite ($CaCO_3$) by acidic solutions (HCl), as follows

$$CaCO_{3(s)} + 2HCl_{(aq)} \rightarrow CaCl_{2(aq)} + CO_{2(aq)} + H_2O_{(l)}. \tag{10}$$
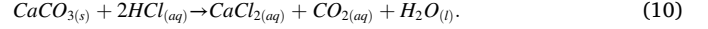
Because the acid is the only component in the aqueous phase that reacts with the solid mineral, it is the only chemical species concentration that needs to be tracked. Note that the rate-limiting reaction is the acid attack on calcite, and it is assumed that carbonate equilibria is totally shifted toward $CO_{2(aq)}$ due to the significant acid concentration in the system. Thus, a single reaction rate is enough to represent our problem. This approach follows from previous literature (Budek and Szymczak, 2012; Tansey and Balhoff, 2016; Soulaine et al., 2017; Esteves et al., 2020).

2.4. Volume evolution and geometry update

As our solution involves geometry changes at each time step, control volumes of pores and throats are changed. In this way, at each time step, with the solution of the concentration field based on mass balance, the change in volume of the pore spaces is obtained by relating the solid volume consumed on the effective surface of each pore space to the density of the reactive mineral that composes the porous medium.

Considering (i) a first-order reaction rate for the heterogeneous chemical reaction, and (ii) a stoichiometric coefficient (β) that relates the consumption of the hydrochloric acid ($\alpha = a$) to the consumption of the reactive mineral, the change in volume due to the dissolution process is given by

$$\delta V_i^d \simeq \frac{R_{a,i} A_{\psi,i}^n \beta \delta t}{\rho_s} = \frac{\left(k_r C_{a,i}^{n+1,*}\right) A_{\psi,i}^n \beta \delta t}{\rho_s}, \tag{11}$$

$$\delta V_{ij}^d \simeq \frac{R_{a,ij} A_{\psi,ij}^n \beta \delta t}{\rho_s} = \frac{\left(k_r C_{a,ij}^{n+1,*}\right) A_{\psi,ij}^n \beta \delta t}{\rho_s}, \tag{12}$$

where $C_{a,i}^{n+1,*}$ and $C_{a,ij}^{n+1,*}$ are the acid concentration in pore i and throat ij, respectively, after the solution of the mass transport in the network, δV_i^d is the change in volume due to dissolution process in pore i, δV_{ij}^d is the change in volume due to dissolution process in throat ij, and ρ_s is the density of the solid phase.

Based on Eqs. (11) and (12), the change in the radii of pores (δr_i^d) and throats (δr_{ij}^d) due to dissolution is defined, respectively, as

$$\delta r_i^d = \frac{\delta V_i^d}{A_{\psi,i}^n} = \frac{k_r C_{a,i}^{n+1,*} \beta \delta t}{\rho_s}, \tag{13}$$

$$\delta r_{ij}^d = \frac{\delta V_{ij}^d}{A_{\psi,ij}^n} = \frac{k_r C_{a,ij}^{n+1,*} \beta \delta t}{\rho_s}. \tag{14}$$

In this algorithm, there are regions in the contact area between pore i and connecting throats ij that are dissolved twice. That is, portions of the pore i and the throat ij are dissolved simultaneously during δt (see Fig. 1, hatched area in red). This consumed volume needs to be counted twice to keep the conservation of mass. For this, the volume related to this region, derived from the dissolution of throat ij, is transferred to the pore i. The change in volume due to double dissolution is then defined by

$$\delta V_{i,ij}^{dd} = \pi \left[\left(r_{ij}^n + \delta r_{ij}^d\right)^2 - \left(r_{ij}^n\right)^2\right] \delta r_i^d. \tag{15}$$

For throats, the double dissolution considers the contact area

between the two connected pores *i* and *j* (see Eq. (16)), and for pores, the double dissolution may account for the contact area between pore *i* and all connected throats *ij* (see Eq. (17)).

$$\delta V_{ij}^{dd} = \delta V_{i,ij}^{dd} + \delta V_{j,ij}^{dd}, \tag{16}$$

$$\delta V_i^{dd} = \sum_{ij} \delta V_{i,ij}^{dd}. \tag{17}$$

The change in radius of pore *i* due to the double dissolution is defined by

$$\delta r_i^{dd} = \frac{\delta V_i^{dd}}{A_{\psi,i}^n}. \tag{18}$$

The grain region that pore *i* invades due to the addition of the double dissolved volumes that is also invaded by the dissolution of throat *ij* (see Fig. 1, hatched area in green) is also transferred for the pore. The volumes related to this region are defined by Eq. (19). The total change in volume related to this step for throats and pores are defined, respectively in Eqs. (20) and (21).

$$\delta V_{i,ij}^{c1} = \pi \left[\left(r_{ij}^n + \delta r_{ij}^d \right)^2 - \left(r_{ij}^n \right)^2 \right] \delta r_i^{dd}. \tag{19}$$

$$\delta V_{ij}^{c1} = \delta V_{i,ij}^{c1} + \delta V_{j,ij}^{c1}. \tag{20}$$

$$\delta V_i^{c1} = \sum_{ij} \delta V_{i,ij}^{c1}. \tag{21}$$

The change in radius of pore *i* due to this first correction step is defined by

$$\delta r_i^{c1} = \frac{\delta V_i^{c1}}{A_{\psi,i}^n}. \tag{22}$$

Again, the grain region that pore *i* invades due to the addition of the correction volume $\delta V_{i,ij}^{c1}$ that is also invaded by the dissolution of throat *ij* (see Fig. 1, hatched area in blue) is transferred to the pore. The volumes related to this region are defined by Eq. (23). The total change in volume related to this step for throats and pores are defined, respectively in Eqs. (24) and (25).

$$\delta V_{i,ij}^{c2} = \pi \left[\left(r_{ij}^n + \delta r_{ij}^d \right)^2 - \left(r_{ij}^n \right)^2 \right] \delta r_i^{c1}. \tag{23}$$

$$\delta V_{ij}^{c2} = \delta V_{i,ij}^{c2} + \delta V_{j,ij}^{c2}. \tag{24}$$

$$\delta V_i^{c2} = \sum_{ij} \delta V_{i,ij}^{c2}. \tag{25}$$

The change in radius of pore *i* due to the this second correction step is defined by

$$\delta r_i^{c2} = \frac{\delta V_i^{c2}}{A_{\psi,i}^n}. \tag{26}$$

Formally, the transfer of volumes between pores and throats requires an iterative process to achieve a desired level of accuracy. Here, the correction step stops in the second iteration because its magnitude is already rather small. For example, for a pore and a throat with diameters equal to 1 and 0.25, respectively, that had an increase of 0.2, the relative error of the final volume of the pore after the second iteration compared to 10 more iterations is 0.00006%.

Finally, pore *i* invades a porous region previously belonging to throat *ij* (see Fig. 1, hatched area in purple). For this case, not only the volume but also the mass of acid that previously belonged to throat *ij* needs to be transferred to pore *i*. Considering this, the transferred porous volume and mass of acid from throat *ij* to pore *i* are defined, respectively, by

$$\delta V_{i,ij}^t = \left(\delta r_i^d + \delta r_i^{dd} + \delta r_i^{c1} + \delta r_i^{c2} \right) A_{i,ij}^n, \tag{27}$$

$$\delta m_{i,ij}^t = C_{ij}^{n+1,*} \left(\delta r_i^d + \delta r_i^{dd} + \delta r_i^{c1} + \delta r_i^{c2} \right) A_{i,ij}^n. \tag{28}$$

where $A_{i,ij}^n$ is the spherical cap area between the pore *i* and throat *ij* at t^n, that is given by Eq. (A.14).

The total change in volume related to this step for throats and pores are defined, respectively, in Eqs. (29) and (30).

$$\delta V_{ij}^t = \delta V_{i,ij}^t + \delta V_{j,ij}^t. \tag{29}$$

$$\delta V_i^t = \sum_{ij} \delta V_{i,ij}^t. \tag{30}$$

The total change in mass of acid related to this step for throats and pores are defined, respectively, in Eqs. (31) and (32).

$$\delta m_{ij}^t = \delta m_{i,ij}^t + \delta m_{j,ij}^t. \tag{31}$$

$$\delta m_i^t = \sum_{ij} \delta m_{i,ij}^t. \tag{32}$$

Fig. 1 presents a schematic of the transferred volumes described previously in this section and Appendix A presents the algorithm for the volume evolution and geometry update. Note that, some controls on the numerical scheme were implemented, as follows. The ratio of the change of throat radius due to dissolution (δr_{ij}^d) to the throat radius from the previous time step was always kept smaller than 0.1 in order to keep a good approximation of the differentials. Also, the Courant numbers (defined as the ratio of the inlet velocity multiplied by the time step to the average length of throats) in all simulations ranged from 0.11 to 1.34. Importantly, all transport-limited conditions were simulated using Courant numbers smaller than 1. These control strategies make the use of 2 iterations to account for the double dissolution accurate to within about 1 part per million as compared to fully converged simulations.

2.5. Pore-merging methodology

This section presents the methodology developed to consider merging of pores and throats during reactive transport simulations when pore surfaces dissolve. The novel merging approach methodology, introduces the use of correction factors to conserve effective surface areas and conductances during the merging process.

In this way, the strategy for merging of pores and throats presented here aims to conserve not only the volume and the mass balance in the system, before and after the application of the merging method, but also the reactive surface areas and conductances. These are key parameters for the reactive transport problem that depends strongly on flow properties (conductance of throats) and features related to the reactivity of the system (reactive surface area).

The idea is to consider an effective surface area and an effective conductance as the parameters necessary to solve the reactive transport problem. In other words, the idea is to replace the area and conductance originally obtained by an effective surface area and conductance that considers approximately the deformation of the pore spaces upon merging.

For this, correction factors are introduced to conserve the effective surface area and effective conductance during the merging process. Therefore, ψ is introduced as the correction factor for surface areas and ϵ is introduced as the correction factor for conductance.

Effective surface area of pores and throats were defined previously in this section by Eqs. (6) and (7). Effective conductance of throats are defined by Eq. (3).

Considering this, original pores and throats have correction factors equal to 1. So, the effective surface areas and effective conductances have the same value as the surface areas and conductances of the pores spaces.

Newly merged pores as well as pores and throats connected to the new merged pores have correction factors different from one to account
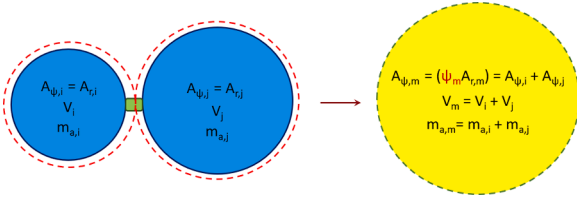
Fig. 2. Two original pores are replaced by one new pore, that has the same total volume, total mass of acid, and total effective surface area as the two original pores.
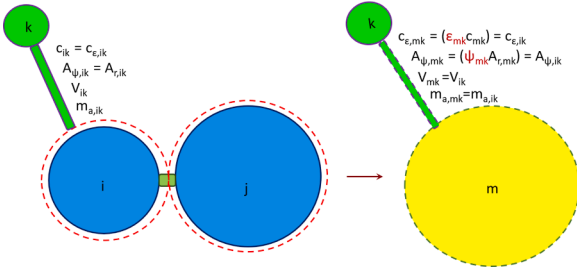

Fig. 3. Pore i and j merge to become pore m. The volume, the mass of acid, the effective surface area, and the effective conductance are conserved for the new throat connecting the merged pore m and the connected pore k.
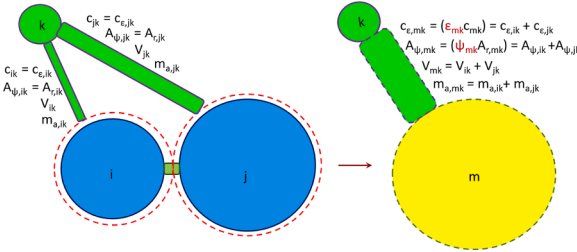

Fig. 4. The merging pores are connected to the same pore k. In this case, one new throat, with the same total volume, mass of acid, effective surface area, and effective conductance as the two original throats, is created.

for the geometric deformations arising from the assumptions of the merge method and, in this way, conserve the effective surface areas and effective conductances during the merging process.

Here, the merging method is performed when two connected pores reach each other and, also, when a throat diameter reaches the same value of the diameter of a connected pore at the end of the geometry update due to dissolution at each time step.

The main steps of this novel merging methodology are then described. The method is explained considering the case of the overlapping pores, but it is similar for the case of throats with larger diameters than the connected pores.

During the merging process, when the merging condition is satisfied, the two original pores are replaced by one new pore with volume, mass of acid, and effective surface area equal to the sum of the corresponding properties of the two original pores (see Fig. 2).

The new merged pore is located in the volume-weighted average of the coordinates of the connecting pores, as presented below

$$\mathbf{x_m^{n+1}} = \frac{V_i^{n+1}\mathbf{x_i^{n+1}} + V_j^{n+1}\mathbf{x_j^{n+1}}}{V_m^{n+1}}, \tag{33}$$

where $\mathbf{x_m^{n+1}}$, $\mathbf{x_i^{n+1}}$, $\mathbf{x_j^{n+1}}$ are the position vectors of the merged pore m and the merging pores i and j, respectively. The volume of the newly merged pore is given by

$$V_m^{n+1} = V_i^{n+1} + V_j^{n+1}. \tag{34}$$

The new radius of the merged pore r_m^{n+1} is obtained by

$$r_m^{n+1} = \sqrt[3]{\frac{3V_m^{n+1}}{4\pi}}. \tag{35}$$

The length of a throat connected to the new merged pore (l_{mk}^{n+1}) is updated due to the location of the merged pore by

$$l_{mk}^{n+1} = d_{mk}^{n+1} - r_m^{n+1} - r_k^{n+1}, \tag{36}$$

where d_{mk}^{n+1} is the interpore distance between the newly merged pore m and the connected pore k, as follows

$$d_{mk}^{n+1} = \left|\mathbf{x_m^{n+1}} - \mathbf{x_k^{n+1}}\right|, \tag{37}$$

where $\mathbf{x_m^{n+1}}$ and $\mathbf{x_k^{n+1}}$ are the position vectors of pores m and k.

There are two different procedures in generating the throats connected to the newly merged pore. The first one applies to throats that connected pores i and j to a third pore that is not simultaneously connected to pores i and j. In this case, the throat properties just have to be updated. Otherwise, throat merging is carried out.

For the first procedure, the throats connected to the merged pore have the same volume, mass of acid, effective surface area, and effective conductance as before the merging process. In this way, the radii of the throats connected to the newly merged pore are updated considering their current volume and the new length, by

$$r_{mk}^{n+1} = \sqrt[2]{\frac{V_{mk}^{n+1}}{\pi l_{mk}^{n+1}}}. \tag{38}$$

The deformation of the throats during the merging process change the reactive surface area and conductance (see Fig. 3). The new surface area and conductance of the throats involved in the merging process, are determined, respectively by

$$A_{r,mk}^{n+1} = 2\pi r_{mk}^{n+1} l_{mk}^{n+1}, \tag{39}$$

$$c_{mk}^{n+1} = \frac{\pi\left(r_{mk}^{n+1}\right)^4}{8\mu l_{mk}^{n+1}}. \tag{40}$$

At this stage, the correction factors for the surface area (ψ_{mk}) and for the conductance (ϵ_{mk}) are updated to maintain the correct effective surface areas and effective conductances of the throats during the merging process, by

$$\psi_{mk}^{n+1} = \frac{A_{\psi,ik}^{n+1}}{A_{r,mk}^{n+1}}, \tag{41}$$

$$\epsilon_{mk}^{n+1} = \frac{c_{\epsilon,ik}^{n+1}}{c_{mk}^{n+1}}. \tag{42}$$

If the original merging pores were connected to the same pore, one new merged throat replaces the two original throats. So, the merged throat connected to the merged pore keeps the sum of the volume, mass of acid, effective surface area, and conductance of the replaced throats (see Fig. 4). The new throat length, radius, effective surface area, and effective conductance are also computed from Eqs. (36), (38), (39), and (40). Consequently, the correction factors are defined as

$$\psi_{mk}^{n+1} = \frac{A_{\psi,ik}^{n+1} + A_{\psi,jk}^{n+1}}{A_{r,mk}^{n+1}}, \tag{43}$$

$$\epsilon_{mk}^{n+1} = \frac{c_{\epsilon,ik}^{n+1} + c_{\epsilon,ik}^{n+1}}{c_{mk}^{n+1}}. \tag{44}$$

Finally, the reactive surface area of the new merged pore is updated considering its new radius (r_m^{n+1}) and the new radii of the connected
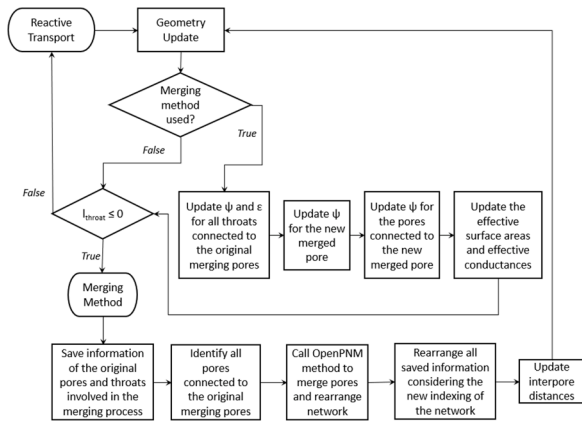
Fig. 5. Flowchart of the novel methodology for merging of pores and throats.

throats, using Eq. (A.15). Then, the correction factor to maintain the correct effective surface area during the merging process is obtained by

$$\psi_m^{n+1} = \frac{A_{\psi,i}^{n+1} + A_{\psi,j}^{n+1}}{A_{r,m}^{n+1}}. \tag{45}$$

Note that the pores connected to the new merged pore also need their effective surface areas updated due to the changes in the radii of the connected throats during the merging process.

The merging approach presented here uses the merging method available within OpenPNM (Gostick et al., 2016) to update the topology of the network. The method creates a new pore to replace the two original pores that are merging, deletes all throats connected to the two original pores, and creates new throats connecting the new merged pore to the pores previously connected to the original merging pores. Considering this, data from all pores and throats involved in the merging process are identified and saved before calling the merge method from OpenPNM and then relocated to the new pores and throats.

Fig. 5 presents a flowchart with the main steps of the novel merging methodology and Appendix B presents the algorithm for the new pore-merging methodology. It should be emphasized that, although the simple stick-and-ball pore-network model was used to model initially the porous medium, the pore and throat shapes become abstract due to the merging process.

2.6. Dimensionless numbers

The use of dimensionless numbers in reactive transport aims to generalize predictions and results across a range of transport and reaction rate conditions. Problems involving reactive transport usually take into account Reynolds (*Re*), Péclet (*Pe*), Damköhler (*Da*) and Péclet-Damköhler (*PeDa*) numbers to characterize different dissolution patterns. The definitions used in this work follow from Soulaine et al. (2017), are calculated at the initial time, and presented below

$$Re = \frac{\rho_f v_0 \sqrt{K_0}}{\mu_f}, \tag{46}$$

$$Pe = \frac{v_0 \sqrt{K_0}}{\mathscr{D}_\alpha}, \tag{47}$$

$$PeDa = \frac{k_r}{A_{ss} \mathscr{D}_\alpha}, \tag{48}$$

$$Da = \frac{k_r}{v_0 \sqrt{K_0} A_{ss}}, \tag{49}$$

where ρ_f is the fluid density, v_0 is the inlet interstitial velocity, $\sqrt{K_0}$ is the square root of the initial permeability of the porous medium, μ_f is the

fluid dynamic viscosity, $\mathscr{D}_\alpha$ is the diffusion coefficient of species α, k_r is the constant of reaction, and A_{ss} is the specific surface area of the porous medium, defined as the ratio of reactive surface area of all pores and throats to the total porous volume. Note that the *PeDa* is important for diffusion-dominated transport (i.e., at low *Pe*), where dissolution patterns are driven by the competition between diffusion and reaction. *Da* alone is appropriate in discussions involving advection-dominated transport (i.e., at high *Pe*).

2.7. Statistical criteria

Esteves et al. (2020) introduced the use of statistical approaches to classify the dissolution regimes. Here, a novel approach that is more general and considers dimensionless parameters is proposed. The use of dimensionless parameters and the linearity of the transient advective-diffusive reaction problem with respect to the acid concentration guarantee that the values of the proposed parameters do not depend on the initial acid concentration.

The network is partitioned in N_{cs} volumes in the flow direction. More specifically, in this study the networks were partitioned in 10 equally distant sections in the flow direction. Each pore space that has its center within a partition volume it is said to belong to this partition. Thus, some statistical quantities can be calculated for each cross-sectional partition.

The coefficient of variation (*CV*) is a unit-free measure of the dispersion of a data set that uses the standard deviation and the mean values. The CV is used to evaluate the variation of the acid concentration profile within the network. Considering the definition of standard deviation (see Eq. (51)), the CV is determined for each network cross-section partition (CV_{cs}) by Eq. (52), where N_{ps} is the total number of pores and throats (identified by the subscript *ps*, derived from pore space) belonging to partition *cs*, σ_{cs} is the standard deviation of cross section *cs*, $C_{a,ps}$ is the acid concentration of the pore space *ps*, and $\overline{C_{a,cs}}$ is the average concentration of acid of all pore spaces within cross section *cs* (see Eq. (50)). The *CV* for each simulation condition is then defined by Eq. (53), where $\overline{CV_{cs}}$ is the average of all CV_{cs}.

$$\overline{C_{a,cs}} = \frac{1}{N_{ps}} \sum_{ps=1}^{N_{ps}} C_{a,ps}. \tag{50}$$

$$\sigma_{cs} = \sqrt{\frac{1}{N_{ps}} \sum_{ps=1}^{N_{ps}} \left(C_{a,ps} - \overline{C_{a,cs}} \right)^2}. \tag{51}$$

$$CV_{cs} = \frac{\sigma_{cs}}{\overline{C_{a,cs}}}. \tag{52}$$

$$CV = \overline{CV_{cs}} = \frac{1}{N_{cs}} \sum_{cs=1}^{N_{cs}} CV_{cs} \tag{53}$$

The measure of the extension of the acid along the network in the flow direction is characterized by the parameter ΔC, that is defined by Eq. (54), where $C_{a,in}$ is the inlet acid concentration and $C_{a,out}$ is the acid concentration in the outlet pore.

$$\Delta C = \left| \frac{C_{a,in} - C_{a,out}}{C_{a,out}} \right| \tag{54}$$

Hence, these two parameters, *CV* and ΔC are used to identified the dissolution regimes.

The preferential pathways dissolution regime, characterized by the formation of very conductive channels where acid flows preferentially, is identified by a large *CV*. This means that acid concentration of pores and throats within the same cross section varies significantly. The surface dissolution regime is characterized by a more homogeneous spread of the acid along the cross sections perpendicular to the flow and is identified by a small *CV* (small dispersion of the values of acid concentration in each cross section) and a high ΔC. The high ΔC identifies

Table 1

Initial porosity (ϕ_0) and initial absolute permeability (K_0) of the networks used in this study.

Network	ϕ_0 (%)	K_0 (m^2)
40x40	20	1.8×10^{-13}
Random	8	6.5×10^{-14}
Carbonate	8	3.7×10^{-16}

Table 2

Simulation conditions explored based on the dimensionless numbers *Pe*, *Da*, and *PeDa*.

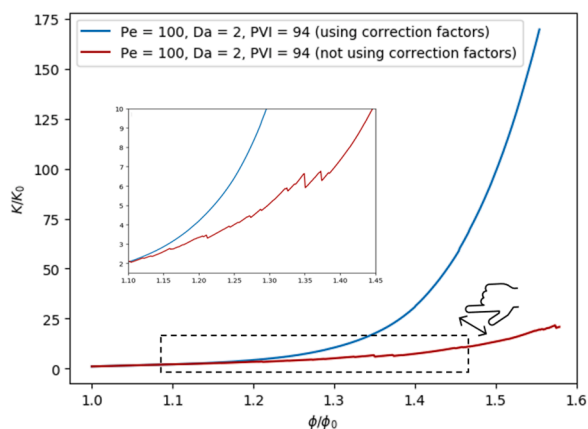| Condition	Expected regime	*Pe*	*Da*	*PeDa*
1	Preferential pathways	100	2	200
2	Surface dissolution	10^{-5}	2	2×10^{-5}
3	Uniform dissolution	100	0.05	5
4	Uniform dissolution	10^{-5}	0.05	5×10^{-7}

Fig. 6. Permeability versus porosity curves obtained for simulations not considering the use of correction factors (red curve) and the use of correction factors (blue curve). The use of correction factors enables a continuous evolution of permeability and porosity of the network under dissolution conditions (see inset that is magnified). The deformation of the original pore spaces due to the merging hypothesis impacts significantly the behavior of the $K - \phi$ curves. (For interpretation of the references to colour in this figure legend, the reader is referred to the web version of this article.)

the consumption of the acid along the network due to the large reactivity of this dissolution regime. Finally, uniform dissolution is described by small values of *CV* and ΔC, that identify a regime that the acid concentration is homogeneous within the cross sections and the consumption is nearly uniform in the entire domain due to the small reactivity of this dissolution regime.

2.8. Pore-network models

Porous media are investigated using two- and three-dimensional (2D and 3D) pore-network models. Pore networks were constructed using OpenPNM (Gostick et al., 2016). The pores are characterized as spherical and are connected to each other by cylindrical throats with circular cross-sections, as appropriate for single-phase flow calculations. Pore walls are assumed to be composed of a single mineral such as calcite.

The two-dimensional cubic network, composed of 40x40 pores, was generated considering a random uniform distribution of pore sizes, in the range of $100 - 300\mu m$. Throat diameters have $1/8$ of the diameter of the smallest pore connected to it and the interpore distances are equal to $300\mu m$.

The random three-dimensional pore network was generated by a method from OpenPNM (Gostick et al., 2016) that creates a random network formed by Gabriel tessellation of arbitrary base points. The size of the pores were defined by a random value between $70\% - 90\%$ of the smallest connected throat interpore distance. Throat diameters have $1/8$ of the diameter of the smallest pore connected to it. The network has a total of 1000 pores, 3447 throats, and an average coordination number of 6.89.

A three-dimensional network was constructed based on the topology information of a carbonate sample. This means that the connectivity between pores, as well as the location of pores and throats in the network, were not generated randomly; instead, they were obtained by mapping the image of the pore spaces of a real carbonate rock sample. The size of the pores were defined by a random value between $60\% - 80\%$ of the smallest connected throat interpore distance. Throat diameters have $1/8$ of the diameter of the smallest pore connected to it. The network has a total of 2612 pores, 5071 throats, and an average coordination number of 3.88.

Table 1 presents the initial porosity (ϕ_0) and initial absolute permeability (K_0) of the networks used in this study.

3. Results and discussion

Simulations of reactive transport and mineral dissolution are performed in different networks to show the applicability of the methodology for a wide range of systems.

Acid with a concentration of $10\,kg/m^3$ is injected from the left-hand side of the network (one-dimensional flow in the positive *x* direction) at a constant volumetric flow rate corresponding to a $Re \approx 0.1$. Fluid and solid properties are set to $\mu_f = 10^{-3}\,Pa.s$, $\rho_f = 1000\,kg/m^3$ and $\rho_{solid} = 2165\,kg/m^3$. The stoichiometric coefficient that relates the consumed acid species with the consumed solid reactive mineral is set to $\beta = 1.37$.

Simulation conditions were explored based on the dimensionless numbers *Pe*, *Da*, and *PeDa* (see Table 2 for details). These numbers were selected to represent the main dissolution regimes (i.e., uniform dissolution, surface dissolution, and preferential pathways) identified in the behavior diagrams presented in our previous work (Esteves et al., 2020). Recall that the uniform dissolution is observed for small *Da* numbers and is characterized by a reaction-limited process. Surface dissolution and the preferential pathways regimes, otherwise, are characterized by transport-limited processes and are highly dependent on *Pe* (Esteves et al., 2020; Golfier et al., 2002).

The inlet velocity was fixed in order to keep *Re* constant and to make the time step the only free parameter necessary to define the Courant number. Hence, reaction rate constant and diffusivity were adjusted to reach the desired values of *Da* and *Pe*, respectively. Alternately, v_0 could have been varied to obtain the desired range of *Pe*, *Da*, and *PeDa*. This alternative procedure was not implemented. The range of k_r and $\mathscr{D}_a$ that were used are $[10^{-4}ms^{-1} - 10^{-2}ms^{-1}]$ and $[10^{-9}m^2s^{-1} - 10^{-2}m^2s^{-1}]$, respectively.

3.1. Effects of using correction factors

The objective of this section is to show the importance of the use of correction factors in stick-and-ball pore network models. One of the main important pieces of information transferred from pore-scale to larger scales is the permeability versus porosity curves. This type of curve is a constitutive relationship for reservoir simulations that relates the evolving permeability based on the increase of the porosity of the porous medium.

Fig. 6 presents an example of the permeability versus porosity curves obtained for simulations not considering the use of the correction factors (in red) and considering the use of correction factors (in blue) in the two-dimensional network under the preferential pathways regime conditions. In a small sample of a completely soluble porous media in the
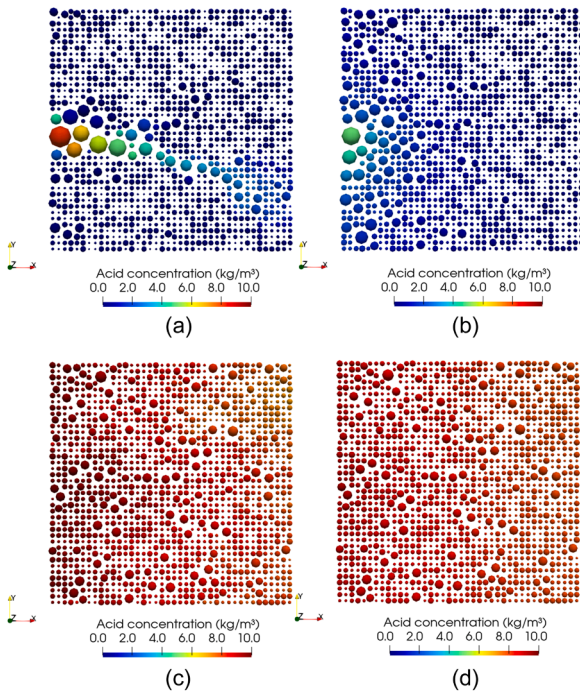
Fig. 7. Acid concentration profile at the end of simulation for the 40x40 network. (a) Case 1, characterized by a preferential pathways regime, after 94 pore volumes injected (PVI). (b) Condition 2, characterized by a surface dissolution regime, after 94 PVI. (c) Conditions 3, characterized by a uniform dissolution regime, after 450 PVI. (d) Condition 4, characterized by a uniform dissolution regime, after 450 PVI.
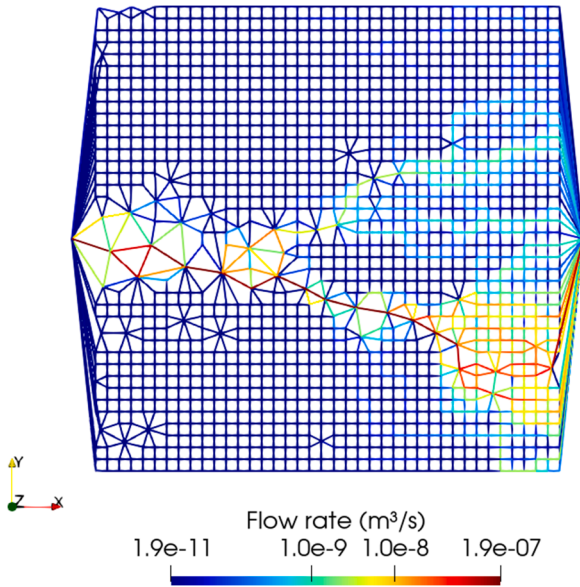

Fig. 8. Flow rate profile for Condition 1, characterized by a preferential pathways regime, after 94 PVI in the 40x40 network. Warmer colors indicate greater velocity.

preferential pathways regime, the acid solution should produce a $K - \phi$ curve that is continuous, smooth, and resembles a power function with a large positive exponent or an exponential function. The $K - \phi$ obtained using the proposed pore merging method with correction factors clearly shows this behavior. The deformation of the original pore spaces due to the merging hypothesis impacts significantly the behavior of the $K - \phi$ curve. Fig. 6 shows that the evolution of permeability is poorly
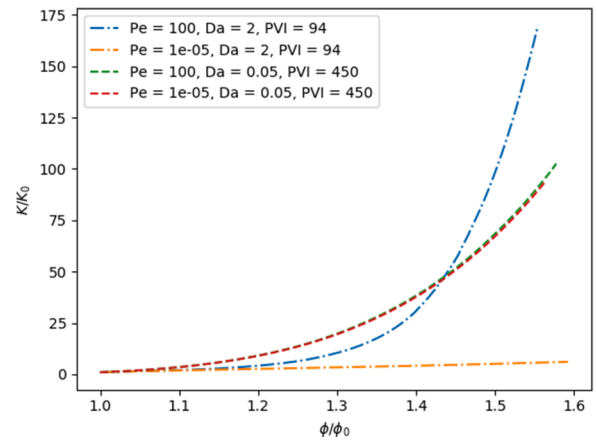

Fig. 9. Permeability versus porosity curves obtained for simulations in the 40x40 network.

represented without using correction factors, as it shows some discontinuities (see inset that is magnified in Fig. 6) and a much smaller permeability increase. This means that, the new methodology proposed here helps in the construction of a more accurate physical description of the evolution of a porous medium under reactive transport and mineral dissolution processes and generates more reliable input information for larger scale simulations.

3.2. Application in a two-dimensional network

This section aims to show the applicability of the methodology for two-dimensional networks. Fig. 7 presents the acid concentration profile at the end of simulations in the 40x40 network. The expected dissolution regime for each simulation condition is observed. Preferential pathways are observed in the middle region of the network for Condition 1 (see Fig. 7a). Surface dissolution is characterized by a homogeneous high acid consumption along the network for Condition 2 (see Fig. 7b). A uniform dissolution regime is observed for Conditions 3 and 4 (see Figs. 7c and 7d) by a uniform and large spread of the acid throughout the entire network. Note that an analysis of the mass balance errors of these simulations, as well as the next simulations discussed in this study, are presented in Appendix C.

Fig. 8 illustrates the complex flow rate profile for Condition 1, characterized by a preferential pathways regime, after 94 PVI in the 40x40 network. The path with the greatest flow rates in the network corroborates the location of the preferential pathways formed during the simulation.

Fig. 9 presents the permeability versus porosity curves obtained for simulations in the 40x40 network. The preferential pathways regime presents the largest increase of the permeability (blue curve) while the surface dissolution presents the largest increase of porosity (orange curve). These behaviors are observed because during the formation of preferential pathways most changes happen through the most permeable flow paths, affecting significantly the overall conductance of the network, whereas during the surface dissolution regime most changes happen nearby the inlet area of the network, increasing the overall porosity, but not the permeability. Uniform dissolution curves (green and red curves) present intermediate behavior. The observed behaviors are expected as previously described in the literature (Egermann et al., 2010; Soulaine et al., 2017; Esteves et al., 2020; Varloteaux et al., 2013).

Besides that, note that the curve of preferential pathways dissolution regime needs more porosity increase than the uniform dissolution curves to reach the largest permeability increase. This fact demonstrates the possible differences in behaviors for networks with different characteristic lengths and the importance to take into account the heterogeneity of the porous medium when discussing results. Also, note that the
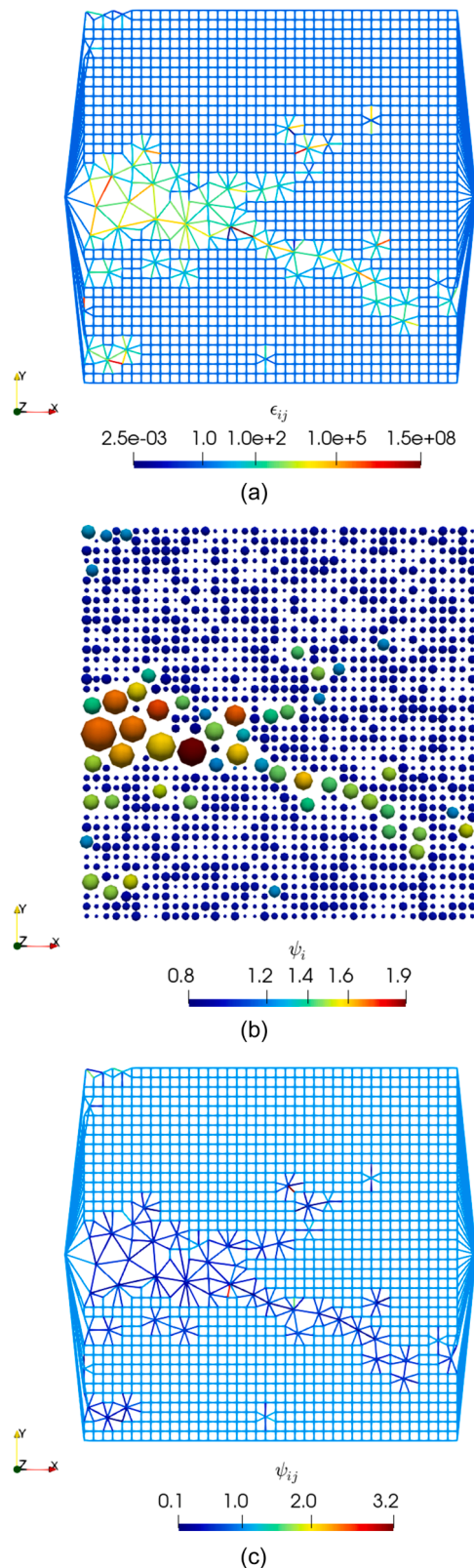
ϵ_{ij}

2.5e-03   1.0 1.0e+2   1.0e+5   1.5e+08

(a)

ψ_i

0.8   1.2 1.4 1.6   1.9

(b)

ψ_{ij}

0.1   1.0   2.0   3.2

(c)

Fig. 10. Final profile of the correction factors considering Condition 1, characterized by a preferential pathways dissolution regime. (a) ψ_i. (b) ψ_{ij}. (c) ϵ_{ij}.

Fig. 11. Acid concentration profile at the end of simulation for the three-dimensional random network. (a) Condition 1, characterized by a preferential pathways regime, after 135 PVI. (b) Condition 2, characterized by a surface dissolution regime, after 135 PVI. (c) Condition 3, characterized by a uniform dissolution regime, after 1212 PVI. (d) Condition 4, characterized by a uniform dissolution regime, after 1212 PVI.
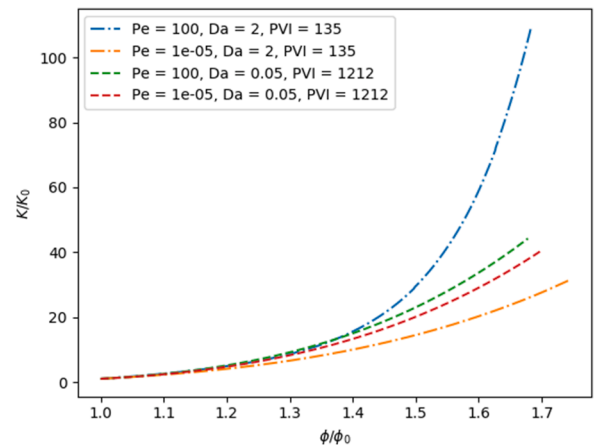
Fig. 12. Permeability versus porosity curves obtained for simulations in the three-dimensional random network.

enabling a more accurate representation of what occurs in real porous media using a simplified stick-and-ball pore-network model.

Additionally, a power-law expression is generally used to represent the relationship between the logarithm of the K/K_0 and the logarithm of ϕ/ϕ_0. Table D.1 from Appendix D presents the power-law exponents and coefficients of determination (R^2) obtained for the simulations in the two-dimensional networks and also for the next simulations presented in this study.

3.2.1. Evolution of correction factors

This section presents the final profile of the correction factors simulating Condition 1, characterized by a preferential pathways dissolution regime, in the 40x40 network (see Fig. 10). The objective

increases observed in Fig. 9 reach values larger than 100 times the initial permeability of the network. These results are possible because of the ability of the algorithm to merge pores and calculate conductance smoothly and accurately during the dissolution of the porous medium,
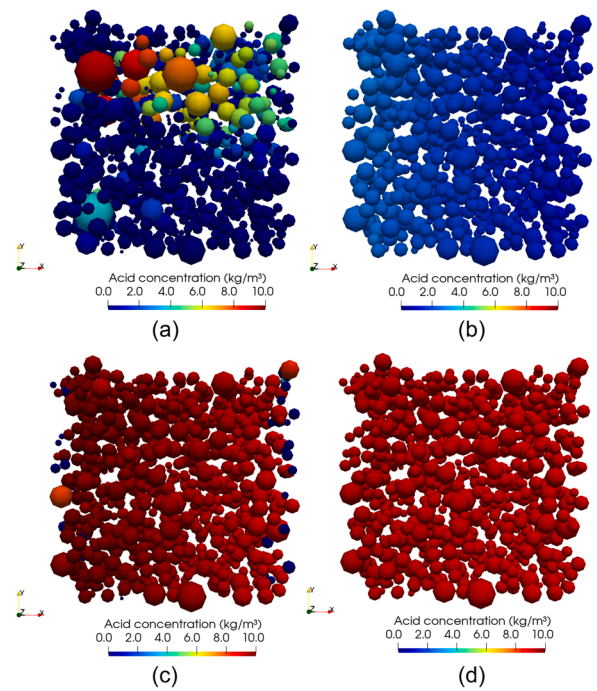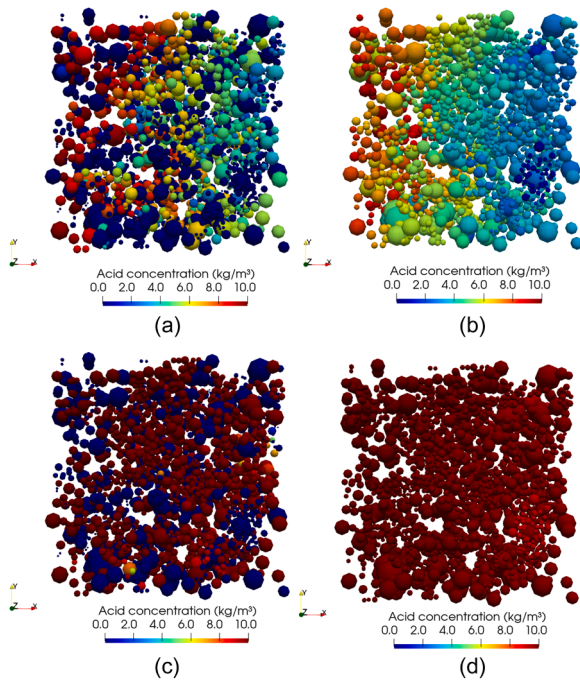
Fig. 13. Acid concentration profile at the end of simulation for the carbonate-derived network. (a) Condition 1, characterized by a preferential pathways regime, after 186 PVI. (b) Condition 2, characterized by a surface dissolution regime, after 139 PVI. (c) Condition 3, characterized by a uniform dissolution regime, after 4182 PVI. (d) Condition 4, characterized by a uniform dissolution regime, after 2788 PVI.
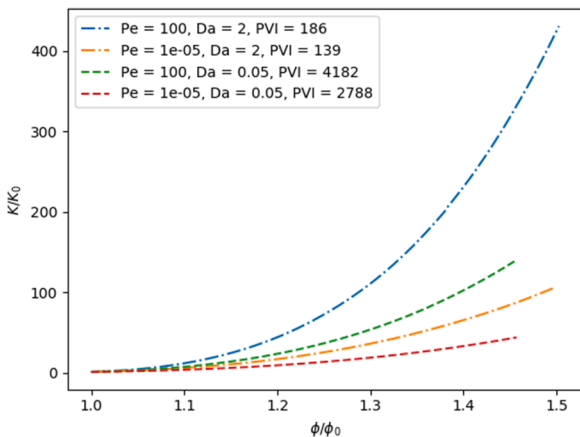

Fig. 14. Permeability versus porosity curves obtained for simulations in the carbonate-derived network.

Table 3
Statistical parameter CV obtained for all the simulation conditions for the three networks explored.

Condition	Observed regime	40x40	Random	Carbonate
1	Preferential pathways	**4.732**	**3.165**	**1.081**
2	Surface dissolution	0.390	0.049	0.219
3	Uniform dissolution	0.093	0.277	0.705
4	Uniform dissolution	0.006	0.001	0.008

here is to show the magnitude of the values necessary to correct the deformation of the pore spaces and conserve the main important properties for the reactive transport and mineral dissolution simulations. Note that modified correction factors are located around the preferential

Table 4
Statistical parameter ΔC obtained for all the simulation conditions for the three networks explored.

Condition	Observed regime	40x40	Random	Carbonate
1	Preferential pathways	5.83	1.95	0.95
2	Surface dissolution	**94.60**	**6.83**	**1.65**
3	Uniform dissolution	0.30	0.12	0.02
4	Uniform dissolution	0.28	0.12	0.03

pathway and the pore spaces that suffered a merging process.

Figs. 10a and 10b present the final profile of the correction factor for the effective surface area of pores (ψ_i) and throats (ψ_{ij}), respectively. The maximum changes for these cases reached approximately one order of magnitude.

Fig. 10c presents the final profile of the correction factor for the effective conductance of throats (ϵ_{ij}). Here, the value of ϵ_{ij} span eleven orders of magnitude. It can be greater than 10^8 times the original values. These results highlight the impact of the deformation of throats on transport during the merging process, that impacts directly the permeability of the network, and the importance in considering correction factors to conserve the evolution of the conductance profile along the network. It should be noted that, being locally defined, the magnitudes of the correction factors do not depend on the network size.

3.3. Three-dimensional network

This section aims to show the applicability of the methodology for simulations in a three-dimensional random network. Fig. 11 presents the acid concentration profile at the end of simulations in the three-dimensional random network. Preferential pathways are observed in the upper region of the network for Condition 1 (see Fig. 11a). Surface dissolution is characterized by a homogeneous high acid consumption along the network for Condition 2 (see Fig. 11b). Uniform dissolution is observed for Conditions 3 and 4 (see Figs. 11c and 11d) by a uniform and significant spread of the acid throughout the entire network. The pores with small acid concentration in Fig. 11c are in the inlet and outlet regions, and are mostly connected to pores in the same region. In this way, they are under the same pressure and, as diffusive transport in this condition is very small, acid couldn't be transported to these specific pores.

Fig. 12 presents the permeability versus porosity curves obtained for simulations in the random network. These results resemble behavior from simulations in the two-dimensional network.

3.4. Carbonate network

This section aims to show the possibility to use the pore merging methodology for very heterogeneous networks. Fig. 13 presents the acid concentration profile at the end of simulations in the carbonate network. The expected dissolution regime for each simulation condition is observed. Here, there is the formation of different preferential pathways due to the significant heterogeneity of the system for Condition 1 (see Fig. 13a). Surface dissolution is characterized by a homogeneous and large acid consumption along the network for Condition 2 (see Fig. 13b). The uniform dissolution regime is observed for Conditions 3 and 4 (see Figs. 13c and 13d) by a large spread of the acid throughout the entire network. Note that there are many pores with small acid concentration in Fig. 13c, Condition 3. This is a consequence of the considerable heterogeneity of this network that presents many restricted pore spaces. Therefore, acid can only reach these pore spaces by diffusion, that occurs at a minimal rate under Condition 3.

Fig. 14 presents the permeability versus porosity curves obtained for simulations in the carbonate network. The general trends are observed, although the curve of the surface dissolution regime (in orange) presents a larger slope than the curve of the uniform dissolution with the same

small Peclet number (in red). This behavior is explained by the small permeability of this network and its significant heterogeneity. There is significant flow resistance in the throats near the inlet region of the network. Thus, the preferential dissolution of this region (characteristic of the surface dissolution) reduces this resistance and promotes the increase of the overall network permeability during the time simulated. Therefore, this slightly odd behavior for the surface dissolution regimes does not occur for the more homogeneous networks previously discussed (see Figs. 9 and 12).

3.5. Statistical parameters analysis

Here, the statistical parameters obtained to] identify the dissolution regimes are presented. Table 3 lists the statistical parameter *CV* and Table 4 presents the statistical parameter ΔC obtained for all the reactive transport and mineral dissolution simulations. Note that the results reflect the final acid concentration profiles and that the increase of porosity for all simulations reached, at least, 40%.

Preferential pathways are identified by the largest values of *CV* and, consequently, the largest variance in the values of acid concentration within each cross section of the network. Based on the simulation results, preferential pathways are identified by $CV > 1$.

Surface dissolution cases are identified by the largest values of ΔC. This means that large acid consumption and large spread of the acid throughout the network are observed. Based on the simulation results, the surface dissolution regime is identified by $\Delta C > 1$.

The uniform dissolution regime is characterized by the smallest values of *CV* and ΔC. This means that reactivity is small and acid spreads homogeneously throughout the entire network. Based on the simulation results, the uniform dissolution regime is identified by both $CV < 1$ and $\Delta C < 1$.

Note that, even for the more complex network topology, the proposed parameters and criteria are able to identify the three main dissolution regimes. This result is obtained despite the presence of significant heterogeneity with greater restrictions to flow and a large number of dead-end pores that make interpretation difficult using simple quantitative criteria. In addition, Appendix E presents quantitative results that demonstrate the adequacy of the proposed criteria for similar regular cubic networks generated with different random seeds. Finally, it is suggested for future studies to obtain the values of these parameters in the region of intermediate *Pe* and *Da* numbers in order to map their trends during regime transition.

4. Conclusions

This study presents a novel pore-network model to simulate single-phase reactive transport and mineral dissolution in porous media. A new methodology for the merging of pores and throats resulting from solid dissolution is introduced to guarantee the conservation of surface areas and throat conductances during the merging process. Pore surface areas and throat conductances are modeled accurately using a novel application of correction factors and effective properties.

A wide range of pore-network models, from a regular two-dimensional network to highly heterogeneous three-dimensional networks, were used to study the reactive transport problem. The main results include the exploration of different dissolution regimes through porosity-permeability evolution curves, acid concentration profiles, and the use of statistical criteria to differentiate regimes. Importantly, this methodology has the ability to simulate permeability increases larger than 100-fold during the formation of preferential pathways through the network.

The innovative approaches presented here may be used to improve the representation of many subsurface applications where reactive transport and mineral dissolution are the fundamental phenomena at the pore-scale, including performance of acidizing for stimulation, geological storage of CO_2, and enhanced oil recovery.

As for future work, a validation exercise is suggested to explore the accuracy of the model using core-flow or micromodel experiments with extensive dissolution for verification. This is an interesting research topic to verify the ability of the algorithm to represent mineral dissolution processes in porous media.

CRediT authorship contribution statement

Barbara F. Esteves: Conceptualization, Software, Writing – original draft. **Paulo L.C. Lage:** Conceptualization, Writing – review & editing. **Paulo Couto:** Funding acquisition, Writing – review & editing. **Anthony R. Kovscek:** Conceptualization, Funding acquisition, Writing – review & editing.

Declaration of Competing Interest

The authors declare that they have no known competing financial interests or personal relationships that could have appeared to influence the work reported in this paper.

Acknowledgments

Appendix A. Algorithm for the volume evolution and geometry update

The steps for the volume evolution and the geometry update of pores and throats are described below.

1. Computation of the change in volume of pores and throats, due to:
   (a) Dissolution (δV_i^d and δV_{ij}^d) using Eqs. (11) and (12),
   (b) Double dissolution (δV_i^{dd} and δV_{ij}^{dd}) using Eqs. (17) and (16),
   (c) The first correction step (δV_i^{c1} and δV_{ij}^{c1}) using Eqs. (21) and (20),
   (d) The second correction step (δV_i^{c2} and δV_{ij}^{c2}) using Eqs. (25) and (24), and
   (e) The transfer of porous spaces (δV_i^t and δV_{ij}^t) using Eqs. (30) and (29).
2. Computation of the total change in volume of pores by

$$\delta V_i = \delta V_i^d + \delta V_i^{dd} + \delta V_i^{c1} + \delta V_i^{c2} + \delta V_i^t \tag{A.1}$$

3. Computation of the total change in volume of throats by

$$\delta V_{ij} = \delta V_{ij}^{d} - \delta V_{ij}^{dd} - \delta V_{ij}^{c1} - \delta V_{ij}^{c2} - \delta V_{ij}^{t} \qquad (A.2)$$

4. Update of the new volume of pores and throats, respectively, by

$$V_{i}^{n+1} = V_{i}^{n} + \delta V_{i}, \qquad (A.3)$$

$$V_{ij}^{n+1} = V_{ij}^{n} + \delta V_{ij}. \qquad (A.4)$$

5. Computation of the change in mass of acid of pores and throats due to the transfer of porous spaces (δm_i^t and δm_{ij}^t) using Eqs. (32) and (31).
6. Computation of the total change in mass of acid inside of pores and throats by

$$m_{i}^{n+1} = \left(C_{i}^{n+1,*} V_{i}^{n} \right) + \delta m_{i}^{t}, \qquad (A.5)$$

$$m_{ij}^{n+1} = \left(C_{ij}^{n+1,*} V_{ij}^{n} \right) - \delta m_{ij}^{t}. \qquad (A.6)$$

7. Update of the acid concentration based on the new volumes obtained by the geometry update, as

$$C_{i}^{n+1} = \frac{m_{i}^{n+1}}{V_{i}^{n+1}}, \qquad (A.7)$$

$$C_{ij}^{n+1} = \frac{m_{ij}^{n+1}}{V_{ij}^{n+1}}. \qquad (A.8)$$

8. Calculation of the new pore radii considering pores as spheres, by

$$r_{i}^{n+1} = \sqrt[3]{\frac{3 V_{i}^{n+1}}{4\pi}}. \qquad (A.9)$$

9. Correction of the new length of throats, by

$$l_{ij}^{n+1} = d_{ij} - r_{i}^{n+1} - r_{j}^{n+1}. \qquad (A.10)$$

10. Calculation of the new throat radii, by

$$r_{ij}^{n+1} = \sqrt[2]{\frac{V_{ij}^{n+1}}{\pi l_{ij}^{n+1}}}. \qquad (A.11)$$

11. Update of the reactive surface area and cross-sectional area of throats, respectively, using

$$A_{r,ij}^{n+1} = 2\pi r_{ij}^{n+1} l_{ij}^{n+1}, \qquad (A.12)$$

$$A_{ij}^{n+1} = \pi \left(r_{ij}^{n+1} \right)^{2}. \qquad (A.13)$$

12. Update the spherical cap areas at the inlet and outlet regions of pore i and determine the reactive surface area, using, respectively

$$A_{i,ij}^{n+1} = 2\pi r_{i}^{n+1} \left(r_{i}^{n+1} - \sqrt{\left(r_{i}^{n+1} \right)^{2} - \left(r_{ij}^{n+1} \right)^{2}} \right) \qquad (A.14)$$

$$A_{r,i}^{n+1} = 4\pi \left(r_{i}^{n+1} \right)^{2} - \sum_{ij} A_{i,ij}^{n+1}, \qquad (A.15)$$

13. Update of the effective surface area of pores and throats using Eqs. (6) and (7).
14. Update of the conductance of throats using Eq. (4).
15. Update of the effective conductance of throats using Eq. (3).

The above procedure is repeated for each time step and, because of this, it is possible to evaluate the evolution of the permeability and porosity during the simulation of the reactive transport coupled with the dissolution process.

Appendix B. Algorithm for the novel pore-merging methodology

The steps of the novel merging approach are described below.

1. Merging condition is satisfied.
2. Save geometric data of all original pores and throats involved in the merging process.
3. Call OpenPNM method for merging of pores and throats.
   Note that this method deletes the two original merging pores and all connected throats and, after that, creates a new merged pore and new connections between the new pore and the previous connected pores. These new pore spaces do not have any geometric information or any data from the mass balance.
4. Update the position of the new merged pore using Eq. (33).
5. Update the radius of the new merged pore and all connected pores using Eq. (35).
6. Update the length of the new throats using Eq. (36).
7. New connected throat radii are obtained by Eq. (38), the surface areas are obtained by Eq. (39), and the conductances are obtained by Eq. (40).
8. Correction factors for the effective surface area and conductance of the connected throats are updated, respectively, using Eqs. (41) and (42). If a new throat replaced two original throats, use Eqs. (43) and (44).
9. Surface areas and correction factors for the effective surface area of the new merged pore and connected pores are updated using Eqs. (A.15) and (45).
10. Effective surface area of pores and throats are updated using Eqs. (6) and 7.
11. Effective conductance of throats are updated using Eq. (3).

Remember that the correction factors are updated just after a change in the topology of the network and that the effective properties are used during the entire simulation for flow and mass balance equations. Thus, for each time step, after the geometry update of the pore spaces, effective properties are determined using the actual correction factors.

Appendix C. Mass balance errors

The mass balance errors are estimated based on the relative difference between the accumulation term and the sum of the terms related to inlet, outlet, and consumption of mass of acid at the end of the simulation, as described bellow

$$MB_{error} = \frac{accumulation - (inlet - outlet - consumption)}{accumulation} \tag{C.16}$$

Table C.1 presents the mass balance errors for the four simulation conditions explored using the three pore-network models explored in this study. The error is presented as a percentage.

Table C.1
Mass balance error (%) obtained in the simulations.

Network	40 × 40	Random	Carbonate
Condition 1	0.0065	0.0014	0.0007
Condition 2	0.0083	0.0014	0.0005
Condition 3	0.0058	0.0038	0.0148
Condition 4	0.0062	0.0038	0.0082

Appendix D. Power-law exponents

Table D.1 presents the power-law exponents and coefficients of determination (R^2) obtained for the simulations in all networks considered in this work.

Generally, the surface dissolution regime (Condition 2) is identified by the smallest power-law exponents. This means that the increase of permeability is limited for a limited porosity variation. Note that in this regime most of the changes in volume occur around the inlet area where most of the acid is already consumed. However, the results for the carbonate network did not follow this trend, as one case with uniform dissolution (Condition 4) showed a smaller power-law coefficient.

The formation of preferential pathways (Condition 1) leads to sharp increases of the permeability for a limited porosity variation and, consequently, is identified by the largest values of the power-law coefficients. The simulation results in the 40x40 network present an exception to this conclusion, and the uniform dissolution cases (Conditions 3 and 4) present the largest values of the exponents. This can be explained by small values of the R^2 that shows that the power-law form can not be the best expression to represent the behavior of the permeability versus permeability curves.

Table D.1
Power-law exponents and coefficients of determination (R^2) obtained for the simulations.

	Exponent (R^2)		
Network	40x40	Random	Carbonate
Condition 1	10.3 (0.953)	8.5 (0.993)	17.2 (0.874)
Condition 2	4.3 (0.902)	6.6 (0.978)	13.1 (0.911)
Condition 3	10.8 (0.981)	7.8 (0.981)	15.1 (0.911)
Condition 4	10.8 (0.982)	7.5 (0.982)	11.1 (0.964)

The uniform dissolution regime (Conditions 3 and 4), in general, presents intermediate behavior of the curves compared to the preferential pathways regime and the surface dissolution regime.

Appendix E. Quantitative criteria in similar networks

Tables E.1 and E.2 present the parameters CV and ΔC, respectively, and their average values and standard deviation obtained by simulating reactive transport and mineral dissolution in different 10x10x10 regular cubic pore-network models. Different initial seeds were used to generate the pore-space sizes and all simulations reached at least 40% increase in porosity. The main objective here is to show the viability of the proposed criteria to identify the main dissolution regimes in similarly constructed networks. The bold values highlight the agreement with the proposed criteria, where the preferential pathways regime is identified by $CV > 1$ while $CV < 1$ and $\Delta C > 1$ characterize the surface dissolution regime. The reported error at the 95% confidence level clearly shows that the regime classification using CV and ΔC does not change within this error range.

Table E.1
Average CV and standard deviation obtained for simulations in different 3D regular cubic networks.

Seeds	Condition 1	Condition 2	Condition 3	Condition 4
17	2.475	0.022	0.233	0.001
77	2.899	0.025	0.227	0.001
100	4.549	0.029	0.230	0.001
1809	4.042	0.034	0.229	0.001
2021	3.298	0.026	0.228	0.001
55	5.449	0.025	0.234	0.001
Average	**3.785**	0.027	0.230	0.001
SD	**1.013**	0.004	0.003	0.000
Error (95%)	**1.164**	0.004	0.003	0.000

Table E.2
Average ΔC and standard deviation obtained for simulations in different 3D regular cubic networks.

Seeds	Condition 1	Condition 2	Condition 3	Condition 4
17	1.304	4.358	0.083	0.083
77	0.934	4.181	0.078	0.078
100	0.662	4.469	0.086	0.086
1809	0.734	4.415	0.084	0.084
2021	0.743	4.280	0.081	0.081
55	0.560	4.270	0.080	0.080
Average	0.823	**4.329**	0.082	0.082
SD	0.242	**0.096**	0.003	0.003
Error (95%)	0.279	**0.111**	0.003	0.000

References

Algive, L., Bekri, S., Vizika, O., 2010. Pore-Network modeling dedicated to the determination of the petrophysical-Property changes in the presence of reactive fluid. SPE J. 15 (03), 618–633. https://doi.org/10.2118/124305-PA.

Bemer, E., Lombard, J.M., 2010. From injectivity to integrity studies of CO_2 geological storage. Oil Gas Sci. Technol. 65 (3), 445–459. https://doi.org/10.2516/ogst/2009028.

Bird, R., Steward, W., Lightfoot, E., 2007. Transport Phenomena. John Wiley and Sons, New York.

Budek, A., Szymczak, P., 2012. Network models of dissolution of porous media. Phys. Rev. E - Stat. Nonlinear Soft Matter Phys. 86 (5), 1–16. https://doi.org/10.1103/PhysRevE.86.056318.

Deng, H., Bielicki, J.M., Oppenheimer, M., Fitts, J.P., Peters, C.A., 2017. Leakage risks of geologic CO_2 storage and the impacts on the global energy system and climate change mitigation. Clim. Change 144 (2), 151–163. https://doi.org/10.1007/s10584-017-2035-8.

Egermann, P., Bekri, S., Vizika, O., 2010. An integrated approach to assess the petrophysical properties of rocks altered by rock-fluid interactions (CO_2 injection). Petrophysics 51 (1), 32–40.

Esteves, B.F., Lage, P.L., Couto, P., Kovscek, A.R., 2020. Pore-network modeling of single-phase reactive transport and dissolution pattern evaluation. Adv. Water Resour. 145 https://doi.org/10.1016/j.advwatres.2020.103741.

Fatt, I., 1956. The network model of porous media. Petroleum Trans. AIME 207, 144–181.

Fredd, C.N., Dowell, S., 2000. Advances in Understanding and Predicting Wormhole Formation, 3. Wiley.

Fredd, C.N., Fogler, H., 1999. Optimum conditions for wormhole formation in carbonate porous media: influence of transport and reaction. SPE J. 4 (03) https://doi.org/10.2118/56995-PA.

Gharbi, O., Bijeljic, B., Boek, E., Blunt, M.J., 2013. Changes in pore structure and connectivity induced by CO_2 injection in carbonates: a combined pore-scale approach. Energy Procedia 37 (0), 5367–5378. https://doi.org/10.1016/j.egypro.2013.06.455.

Golfier, F., Zarcone, C., Bazin, B., Lenormand, R., Lasseux, D., Quintard, M., 2002. On the ability of a darcy-scale model to capture wormhole formation during the dissolution of a porous medium. J. Fluid Mech. 457, 213–254. https://doi.org/10.1017/S0022112002007735.

Gostick, J., Aghighi, M., Hinebaugh, J., Tranter, T., Hoeh, M.A., Day, H., Spellacy, B., Sharqawy, M.H., Bazylak, A., Burns, A., Lehnert, W., Putz, A., 2016. Openpnm: a pore network modeling package. Comput. Sci. Eng. 18 (4), 60–74.

Hill, A.D., Schechter, R.S., 2000. Fundamentals of Acid Stimulation, 3. Wiley.

Huber, C., Shafei, B., Parmigiani, A., 2014. A new pore-scale model for linear and non-linear heterogeneous dissolution and precipitation. Geochim. Cosmochim. Acta 124, 109–130. https://doi.org/10.1016/j.gca.2013.09.003.

Jones, E., Oliphant, T., Peterson, P., et al., 2001. SciPy: Open source scientific tools for Python.

Kang, Q., Zhang, D., Chen, S., He, X., 2002. Lattice boltzmann simulation of chemical dissolution in porous media. Phys. Rev. E - Stat. Phys. Plasmas Fluids Relat. Interdiscip. Topic. 65 (3) https://doi.org/10.1103/PhysRevE.65.036318.

Li, L., Peters, C.A., Celia, M.A., 2006. Upscaling geochemical reaction rates using pore-scale network modeling. Adv. Water Resour. 29 (9), 1351–1370. https://doi.org/10.1016/j.advwatres.2005.10.011.

Liu, M., Mostaghimi, P., 2017. Characterisation of reactive transport in pore-scale correlated porous media. Chem. Eng. Sci. 173, 121–130. https://doi.org/10.1016/j.ces.2017.06.044.

Mehmani, Y., Balhoff, M.T., 2015. Mesoscale and hybrid models of fluid flow and solute transport. Rev. Mineral. Geochem. 80 (1), 433–459. https://doi.org/10.2138/rmg.2015.80.13.

Menke, H.P., Reynolds, C.A., Andrew, M.G., Pereira Nunes, J.P., Bijeljic, B., Blunt, M.J., 2018. 4D Multi-scale imaging of reactive flow in carbonates: assessing the impact of heterogeneity on dissolution regimes using streamlines at multiple length scales. Chem. Geol. 481 (January), 27–37. https://doi.org/10.1016/j.chemgeo.2018.01.016.

Molins, S., Soulaine, C., Prasianakis, N.I., Abbasi, A., Poncet, P., Ladd, A.J., Starchenko, V., Roman, S., Trebotich, D., Tchelepi, H.A., Steefel, C.I., 2020. Simulation of mineral dissolution at the pore scale with evolving fluid-solid interfaces: review of approaches and benchmark problem set. Comput. Geosci. https://doi.org/10.1007/s10596-019-09903-x.

Molins, S., Trebotich, D., Steefel, C.I., Shen, C., 2012. An investigation of the effect of pore scale flow on average geochemical reaction rates using direct numerical simulation. Water Resour. Res. 48 (3), 1–11. https://doi.org/10.1029/2011WR011404.

Oliveira, T.D., Blunt, M.J., Bijeljic, B., 2019. Modelling of multispecies reactive transport on pore-space images. Adv. Water. Resour. 127 (August 2018), 192–208. https://doi.org/10.1016/j.advwatres.2019.03.012.

Ott, H., Oedai, S., 2015. Wormhole formation and compact dissolution in single- and two-phase CO_2-brine injections. Geophys. Res. Lett. 42 (7), 2270–2276. https://doi.org/10.1002/2015GL063582.

Raoof, A., Nick, H.M., Wolterbeek, T.K., Spiers, C.J., 2012. Pore-scale modeling of reactive transport in wellbore cement under CO_2 storage conditions. Int. J. Greenhouse Gas Control 11 (SUPPL), 67–77. https://doi.org/10.1016/j.ijggc.2012.09.012.

Rathnaweera, T.D., Ranjith, P.G., Perera, M.S., 2016. Experimental investigation of geochemical and mineralogical effects of CO_2 sequestration on flow characteristics of reservoir rock in deep saline aquifers. Sci. Rep. 6 (September 2015), 1–12. https://doi.org/10.1038/srep19362.

Sohrabi, M., Kechut, N.I., Riazi, M., Jamiolahmady, M., Ireland, S., Robertson, G., 2012. Coreflooding studies to investigate the potential of carbonated water injection as an injection strategy for improved oil recovery and CO_2 storage. Transp. Porous Media 91 (1), 101–121. https://doi.org/10.1007/s11242-011-9835-5.

Soulaine, C., Roman, S., Kovscek, A., Tchelepi, H.A., 2017. Mineral dissolution and wormholing from a pore-scale perspective. J. Fluid Mech. 827, 457–483. https://doi.org/10.1017/jfm.2017.499.

Tansey, J., Balhoff, M.T., 2016. Pore network modeling of reactive transport and dissolution in porous media. Transp. Porous Media 113 (2), 303–327. https://doi.org/10.1007/s11242-016-0695-x.

Tartakovsky, A.M., Trask, N., Pan, K., Jones, B., Pan, W., Williams, J.R., 2016. Smoothed particle hydrodynamics and its applications for multiphase flow and reactive transport in porous media. Comput. Geosci. 20 (4), 807–834. https://doi.org/10.1007/s10596-015-9468-9.

Varloteaux, C., Békri, S., Adler, P.M., 2013. Pore network modelling to determine the transport properties in presence of a reactive fluid: from pore to reservoir scale. Adv. Water Resour. 53, 87–100. https://doi.org/10.1016/j.advwatres.2012.10.004.

Wolterbeek, T.K., Raoof, A., 2018. Meter-Scale reactive transport modeling of CO_2-Rich fluid flow along debonded wellbore casing-Cement interfaces. Environ. Sci. Technol. 52 (6), 3786–3795. https://doi.org/10.1021/acs.est.7b05358.

Yang, X., Mehmani, Y., Perkins, W.A., Pasquali, A., Schönherr, M., Kim, K., Perego, M., Parks, M.L., Trask, N., Balhoff, M.T., Richmond, M.C., Geier, M., Krafczyk, M., Luo, L.S., Tartakovsky, A.M., Scheibe, T.D., 2016. Intercomparison of 3D pore-scale flow and solute transport simulation methods. Adv. Water Resour. 95, 176–189. https://doi.org/10.1016/j.advwatres.2015.09.015.